Supporting Information

Chain and Condensed State Structure-Directed Fabrication of Dynamic Surface Gratings in Azopolymers for Invisible Patterns and Multi-modal Anti-counterfeiting

Xixi Su,[a] Haifeng Xu,[a] Qi Guo,[a] Runxin Bei,[a] Li Gong,[d] Yuzhao Yang,[b, c*] Zhongke Yuan,[b, c] Shaolin Lu,[b, c] Dengchong Feng,[b, c*] Zishou Zhang,[a] and Xudong Chen[a, b, c*]

[a] *Key Laboratory for Polymeric Composite and Functional Materials of Ministry of Education Guangdong Engineering Technology Research Center for High-performance Organic and Polymer Photoelectric Functional Films, School of Chemistry, Sun Yat-sen University, Guangzhou 510275, China*

[b] *School of Chemical Engineering and Light Industry, Guangdong University of Technology, Guangzhou, 510006, China*

[c] *Guangdong Provincial Laboratory of Chemistry and Fine Chemical Engineering Jieyang Center, Jieyang 515200, China*

[d] *Instrumental Analysis Research Center, Sun Yat-sen University, Guangzhou, China*

E-mail: yangyuzh@gdut.edu.cn; fengdch@gdut.edu.cn; chenxd@gdut.edu.cn

Keywords: multimodal anti-counterfeiting, azobenzene, dynamic gratings, condensed state structure, invisible patterns

Contents

Experimental section: additional notes

Materials

3,5-Dibromophenol, 1,2-Dibromoethane, 1,4-Dibromobutane, 1,8-Dibromooctane, 1,12-Dibromododecane, 4-(Phenyldiazenyl)phenol and (4-Aminophenyl) boronic acid HCl Salt were purchased from Aladdin and used as received. 1,6-Hexanediamine, 1,8-Octanediamine, 4,7,10-Trioxa-1,13-tridecanediamine, 1-(2-Hydroxyethyl)-3,3-dimethylindolino-6'-nitrobenzopyrylospiran were purchased from Macklin and used as received. 4,4'-Oxydianiline (ODA), and Pyromellitic Dianhydride (PMDA) were purchased from Tokyo Chemical Industry Co., Ltd. and used as received. Tetrakis (triphenylphosphine)palladium (0) (Pd $[P(C_6H_5)_3]_4$), N,N-Dimethylacetamide (DMAc) was bought from J&K Scientific and used as received. K_2CO_3, Acetone, Tetrahydrofuran, Petroleum ether and Methylene chloride were purchased from Guangzhou Chemical Reagent Factory.

Details of measuring method

UV-vis absorption spectra were recorded on a Lambda 950 (Perkin Elmer, UK) at room temperature. Reflectance spectra were measured using a spectrometer (Ocean Optics Maya-2000 pro) with an angle-resolved attachment. Fourier transform infrared (FT-IR) spectra were obtained through an infrared spectrometer Frontier (PerkinElmer, America). Gel permeation chromatography (GPC) was conducted with a Waters Model 717 plus autosampler as well as a Waters Model 1515 isocratic HPLC pump. The eluent was DMF with 0.05M LiBr/ 0.1M HAc and relative molecular weight was calibrated with narrow polydispersity polymethyl methacrylate standards. Thermogravimetric analyses (TGA) were measured by a thermal analyzer PE Pyris1 TGA (PerkinElmer, America) at a heating rate of 10 °C·min^{-1} from 30 °C to 450 °C under 40 mL·min^{-1} N_2 flow. Atomic Force Microscope (AFM) was used to measure the microscopic topography and the modulus of the film (Bruker Dimension

Fastscan, Germany). The mechanical properties of the films were measured using dynamic mechanical analysis (DMA) at 25°C (TA-Instruments, America). The microscopic morphology was characterized by an optical microscope (Optec, BK-POL). Digital microscope DSX1000 (Olympus, Japan) was used to test super-depth-of-field microscope images of gratings on the films. The thickness of the films was measured by a surfcorder ET 150 (Kosaka Laboratory Ltd. Japan). The pictures were taken through a Canon camera (EOS RP). Wide-angle X-ray diffraction (WAXD) were measured on an X-ray diffractometer (Rigaku SmartLab, Japan) using Cu Kα (λ = 0.1543 nm) with 40 kV/30mA from 5°to 50° (2θ) and d-spacing was calculated through Bragg's Law.

Molecular dynamics (MD) simulation: MD serves as a powerful tool to investigate and understand the interactions between microscopic particles. All simulations in this study were performed using the Materials Studio software package. The composite structure was constructed using the Amorphous Cell module, which employs the Monte Carlo algorithm to generate random morphologies within a three-dimensional periodic cell. Periodic boundary conditions (PBC) were implemented along all three directions. To prevent local energy accumulation and maintain structural stability, geometry optimization and dynamic simulations of the composite structure were conducted using the Forcite module. An NPT simulation was performed for 2000 ps at 298 K and 0.1 MPa, employing the Nosé thermostat with a Q ratio of 0.01. Both intra- and inter-molecular interactions were described by the COMPASS III force field. The atomic charges were assigned based on the force field parameters. The van der Waals interactions were calculated using atom-based summation, while electrostatic interactions were computed using the particle-particle particle-mesh (PPPM) method. The simulation was conducted with a time step of 1 fs, and trajectory frames were saved every 5000 steps.

Structural confirmation (NMR and HRMS) of intermediates and final products of TP-*n*C-Azo photosensitive monomers

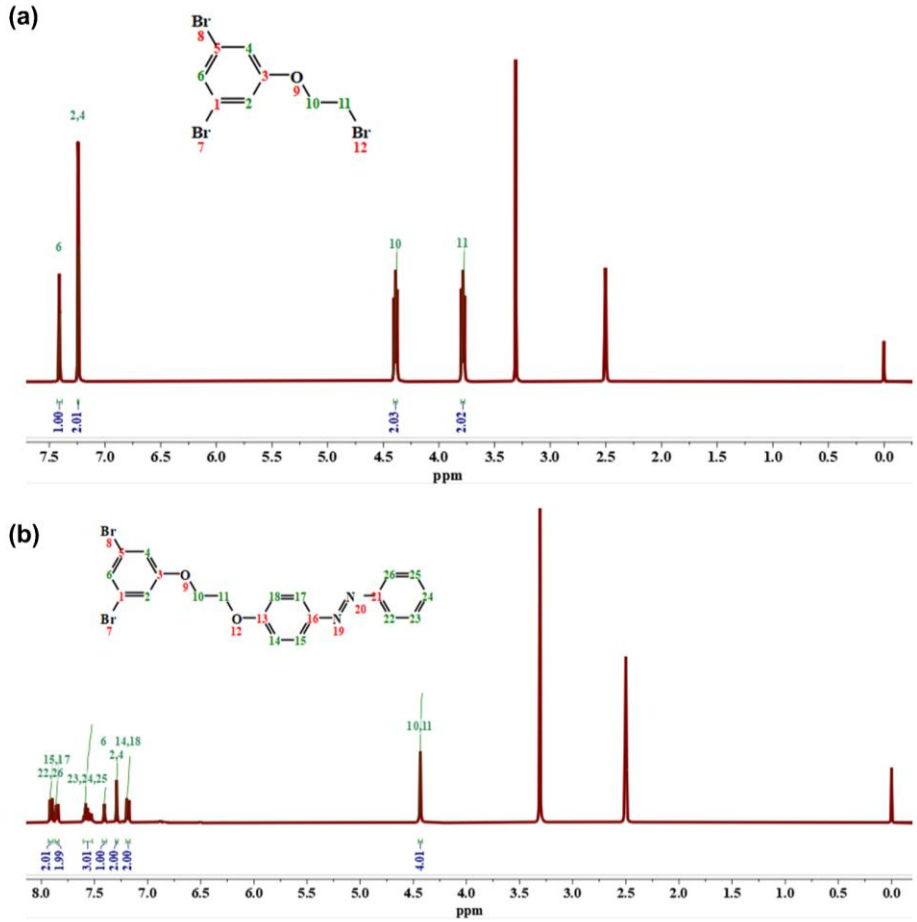

Figure S1. ^{1}H NMR (400 MHz, DMSO-*d*6, δ, ppm) of intermediates B (a) and C (b) in the synthetic route of TP-2C-Azo.

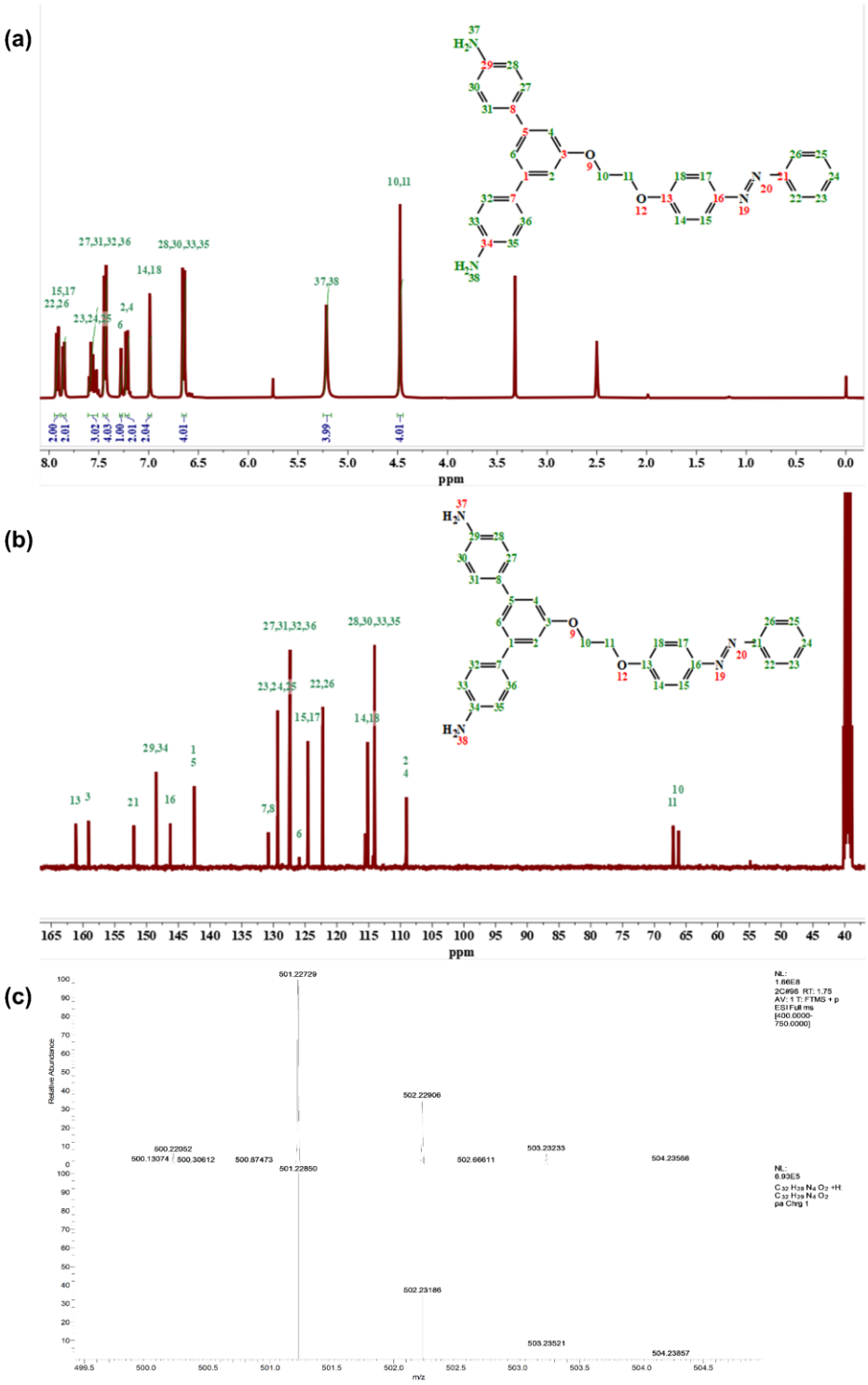

Figure S2. ^{1}H NMR (400 MHz, DMSO-*d*6, *δ*, ppm), ^{13}C NMR (101 MHz, DMSO-*d*6, *δ*, ppm) and HRMS (m/z: $[m+H]^{+}$ calcd for $C_{32}H_{28}N_4O_2$, 501.22850, found 501.22729) of TP-2C-Azo.

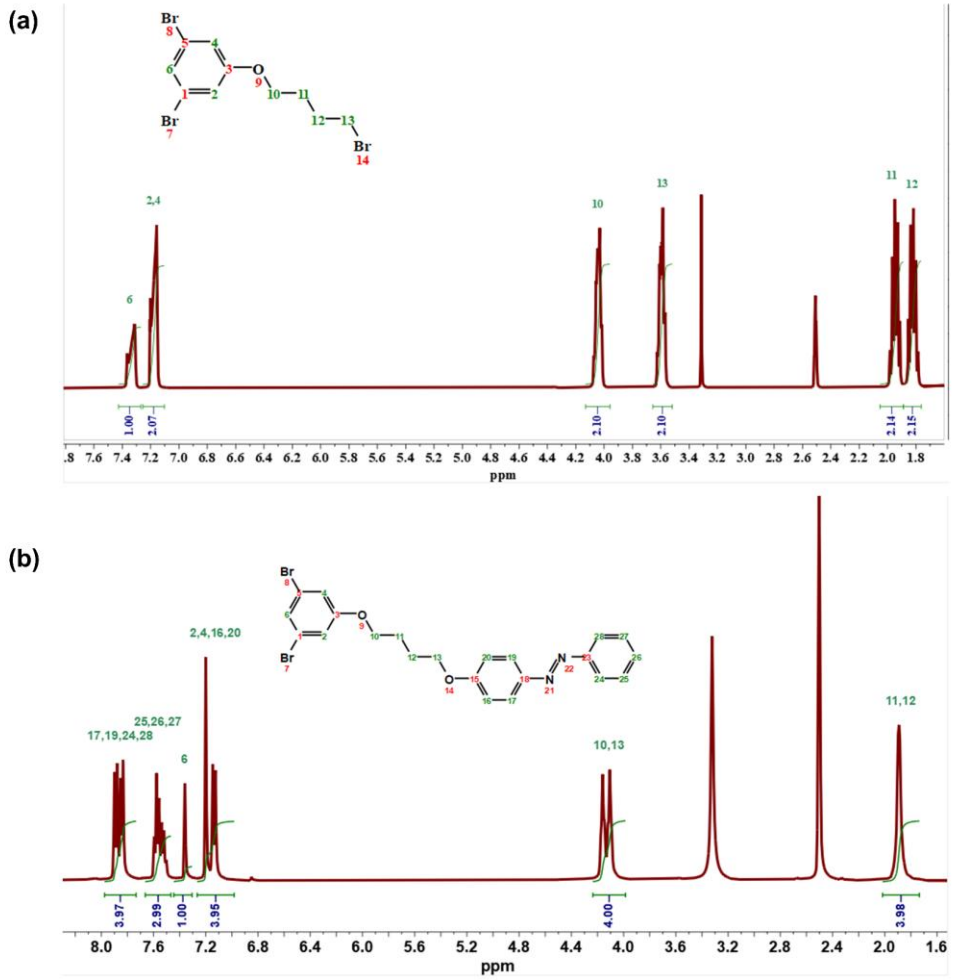

Figure S3. ^{1}H NMR (400 MHz, DMSO-*d*6, δ, ppm) of intermediates B (a) and C (b) in the synthetic route of TP-4C-Azo.

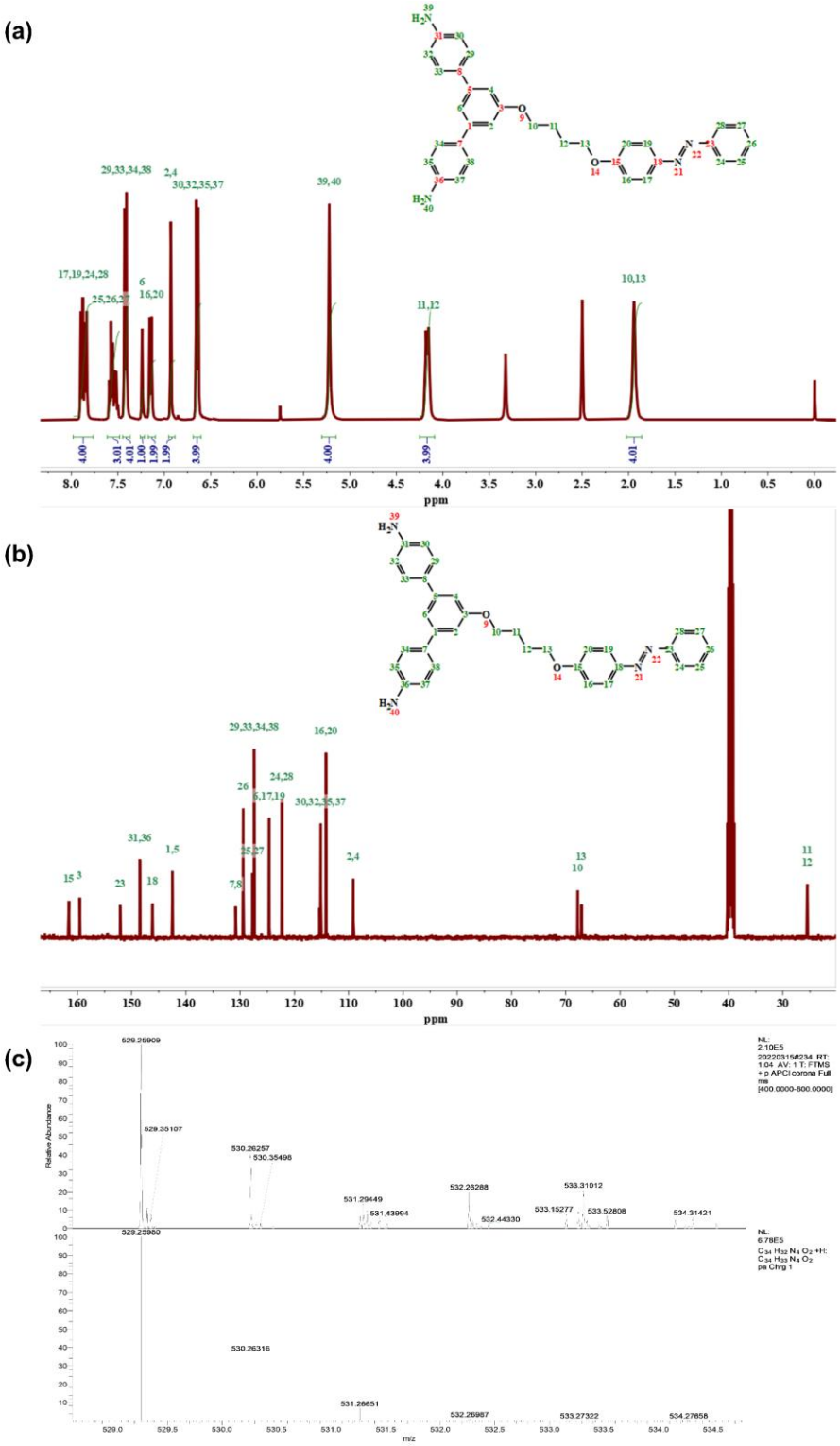

Figure S4. ^{1}H NMR (400 MHz, DMSO-*d*6, *δ*, ppm), ^{13}C NMR (101 MHz, DMSO-*d*6, *δ*, ppm) and HRMS (m/z: $[m+H]^+$ calcd for $C_{34}H_{32}N_4O_2$, 529.25980, found 529.25909) of TP-4C-Azo.

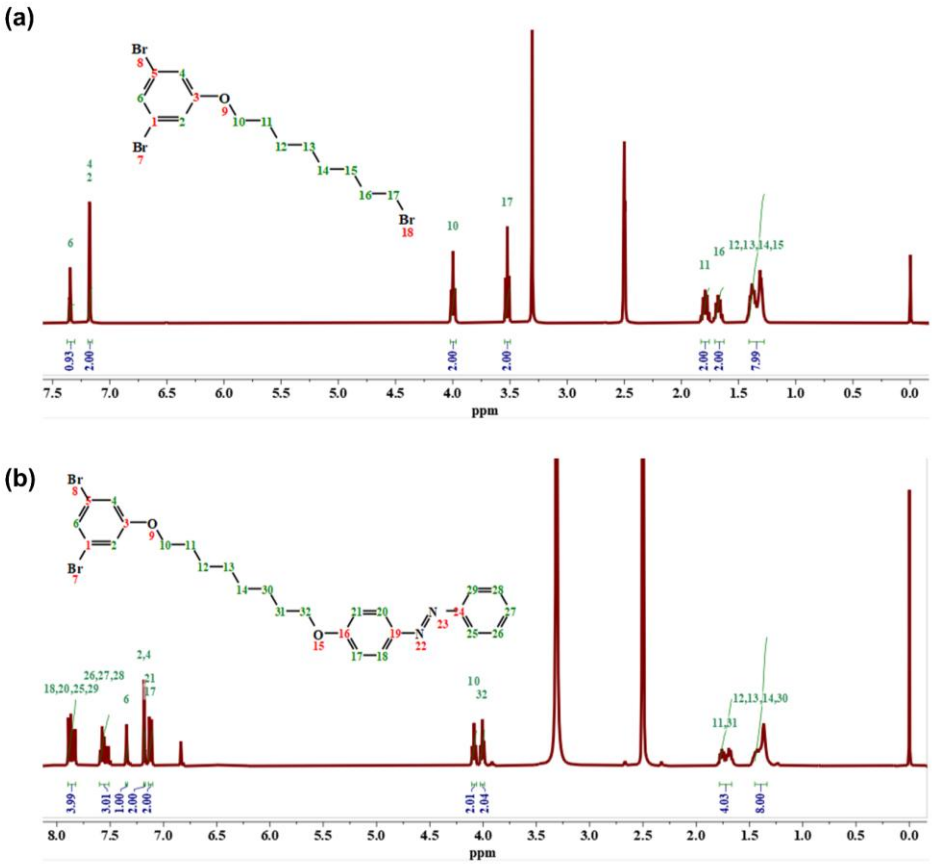

Figure S5. ^{1}H NMR (400 MHz, DMSO-*d*6, *δ*, ppm) of intermediates B (a) and C (b) in the synthetic route of TP-8C-Azo.

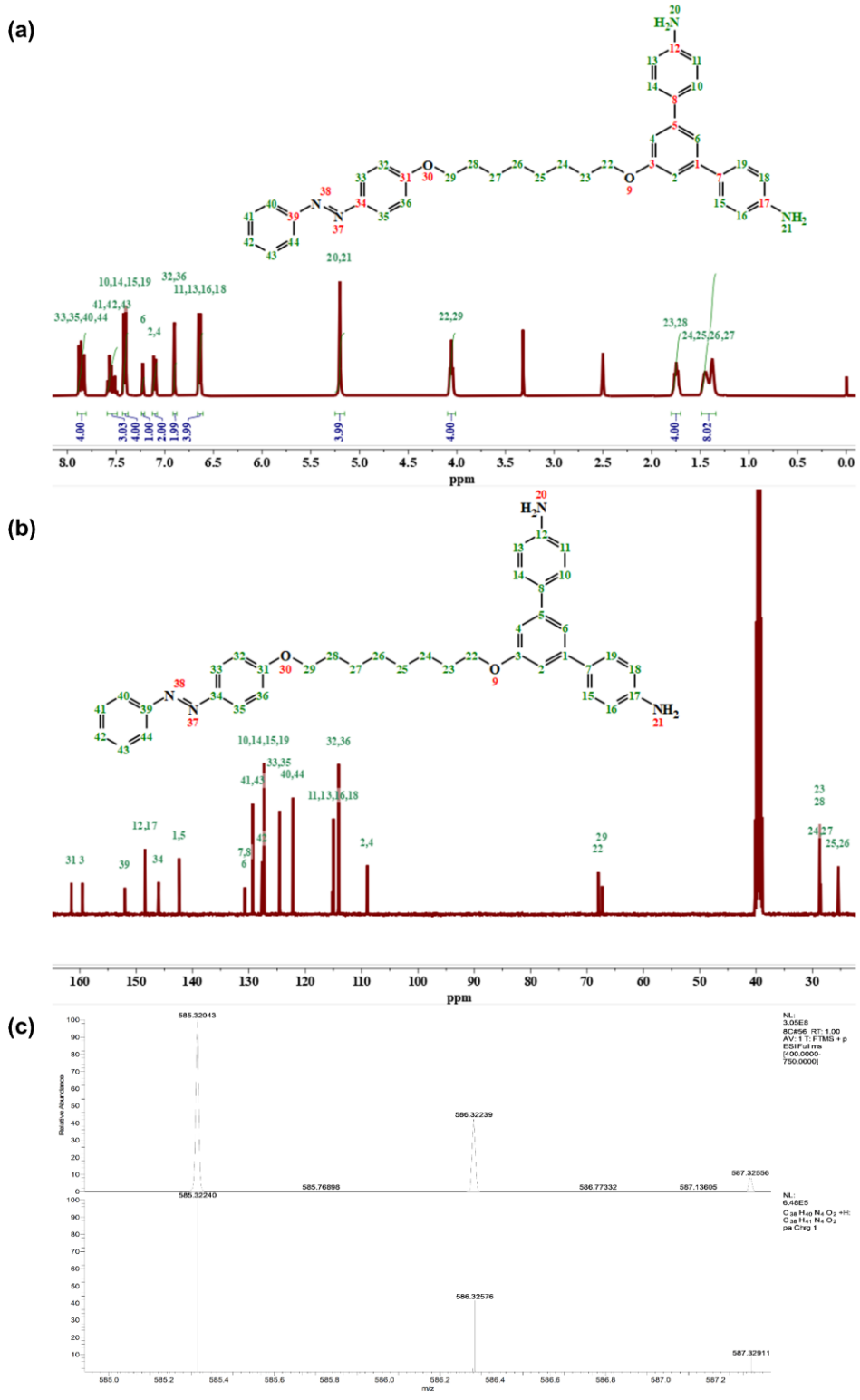

Figure S6. ^{1}H NMR (400 MHz, DMSO-*d*6, *δ*, ppm), ^{13}C NMR (101 MHz, DMSO-*d*6, *δ*, ppm) and HRMS (m/z: $[m+H]^{+}$ calcd for $C_{38}H_{40}N_4O_2$, 585.32240, found 585.32043) of TP-8C-Azo.

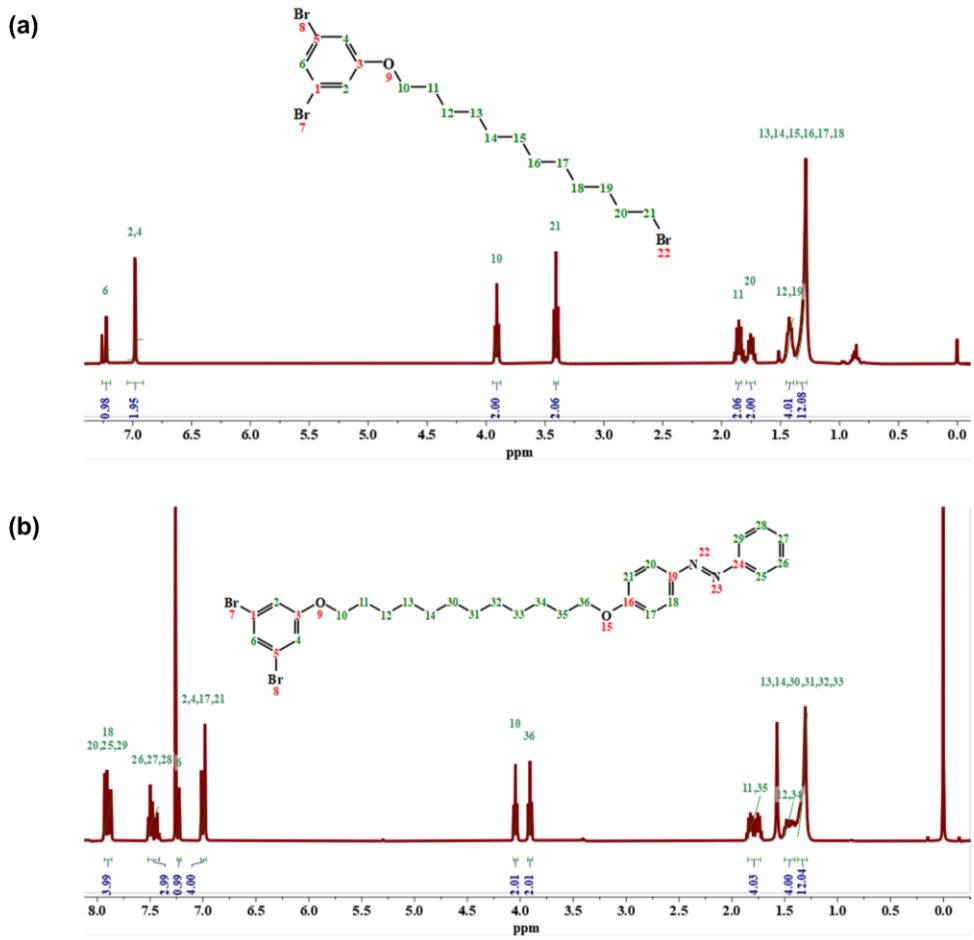

Figure S7. ^{1}H NMR (400 MHz, DMSO-*d*6, *δ*, ppm) of intermediates B (a) and C (b) in the synthetic route of TP-12C-Azo.

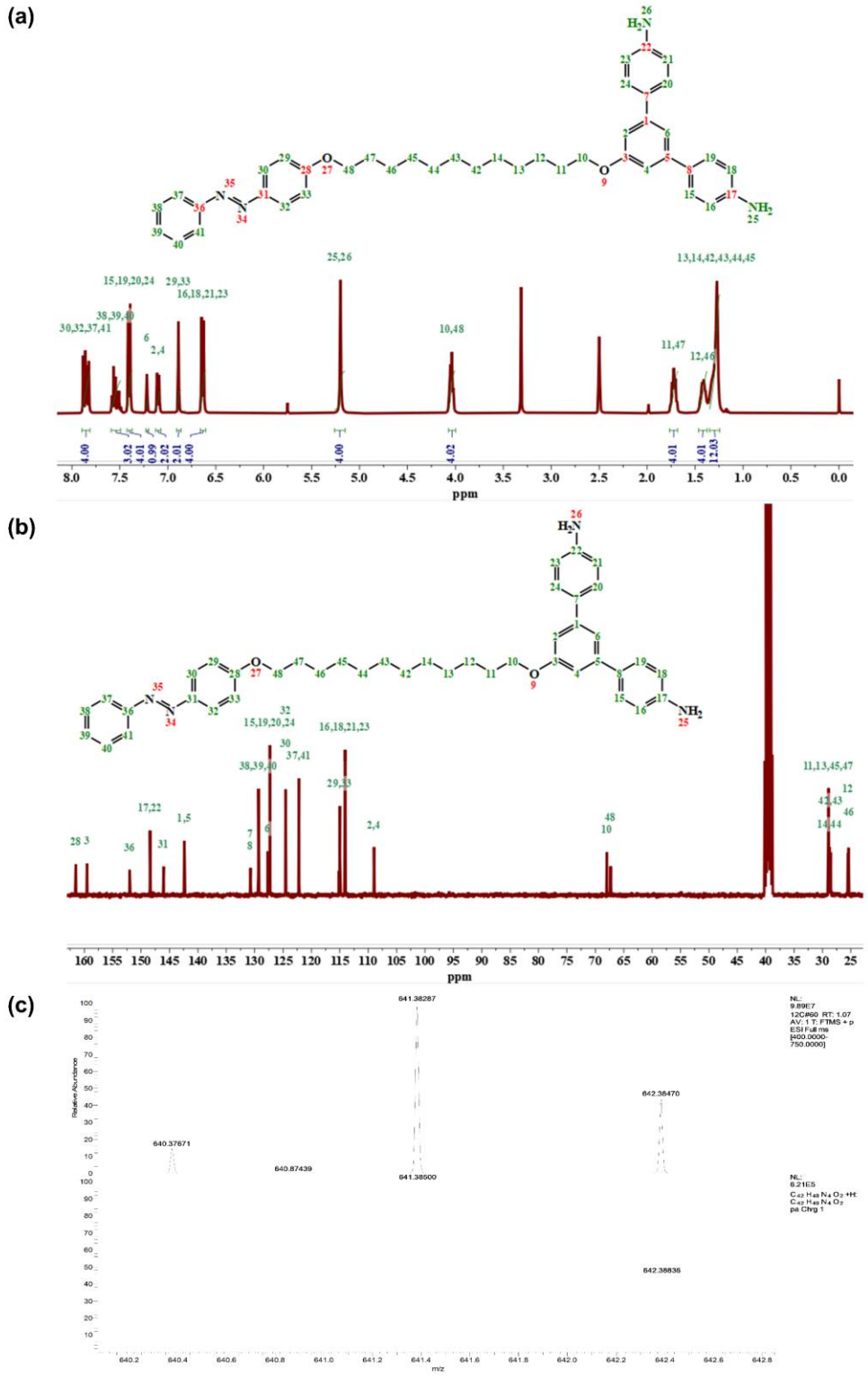

Figure S8. ^{1}H NMR (400 MHz, DMSO-*d*6, *δ*, ppm), ^{13}C NMR (101 MHz, DMSO-*d*6, *δ*, ppm) and HRMS (m/z: $[m+H]^{+}$ calcd for $C_{42}H_{48}N_4O_2$, 641.38500, found 641.38287) of TP-12C-Azo.

The UV-induced isomerization of monomers containing azobenzene (TP-*n*C-Azo)

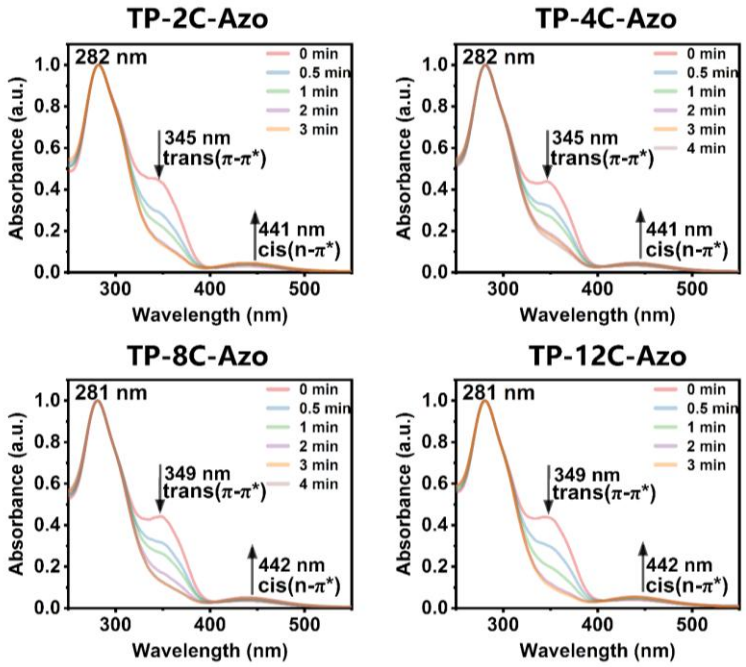

Figure S9. The UV-Vis absorption spectra of TP-*n*C-Azo.

To investigate the photoisomerization behavior of the synthesized TP-*n*C-Azo monomers under UV irradiation, UV-Vis spectroscopy analysis was performed. The UV-Vis absorption spectra of TP-*n*C-Azo under UV light exposure (0.30 mW/cm²) are shown in **Figure S9**. Initially, the azobenzene moieties in TP-*n*C-Azo molecules, predominantly existing in the *trans* configuration, displayed a characteristic strong π-π^* absorption band at 345 nm (or 349 nm) and a weak n-π^* absorption band at 441 nm. Upon continuous UV exposure, the azobenzene functional groups in TP-*n*C-Azo progressively underwent *trans*→*cis* photoisomerization. As the population of *cis* isomers increased, the π-π^* absorption peak corresponding to the trans state diminished, while the n-π^* absorption peak associated with the *cis* state intensified. These spectral changes demonstrate that the synthesized TP-*n*C-Azo monomers efficiently undergo *trans*→*cis* photoisomerization under UV irradiation.

Molecular weight of azobenzene polymers with different side-chain and main-chain structures

Table S1. Molecular weights of azobenzene-containing polymers with various side-chain structures.

Types	M_n	M_w	PDI
2C	30482	36620	1.20
4C	31669	38337	1.21
8C	32932	41250	1.25
12C	35076	44925	1.28

Table S2. Molecular weights of azobenzene polymers with different HMDA contents.

Content(%)	M_n	M_w	PDI
20	27186	35519	1.31
40	24458	37693	1.54
60	25664	37772	1.47
80	23661	33207	1.40
100	19434	28082	1.44

Table S3. Molecular weights of azobenzene polymers with different OADA contents.

Content(%)	M_n	M_w	PDI
20	25416	33917	1.33
40	25582	36708	1.44
60	23663	33745	1.43
80	22193	31614	1.42
100	21163	30993	1.46

Table S4. Molecular weights of azobenzene polymers with different ZF-NH_2 contents.

Content(%)	M_n	M_w	PDI
20	36780	46750	1.27
40	32535	43349	1.33
60	31474	42536	1.35
80	30939	41799	1.35
100	32156	43755	1.36

Investigation of *trans-cis* isomerization kinetics in azobenzene polymer films: synthesis and thickness characterization of Paz films

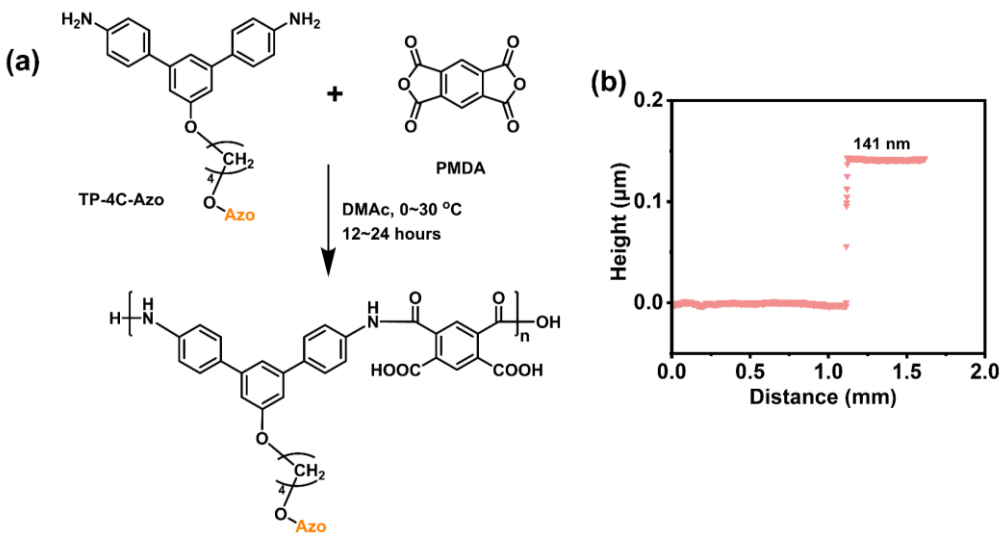

Figure S10. Synthesis scheme of Paz (a) and the thickness of the film after spin coating was measured by a step instrument, and the film thickness was 141 nm (b).

To quantitatively determine the activation energy associated with photoinduced *trans-cis* isomerization in azobenzene-containing polymers, we synthesized an azobenzene polymer (Paz) through the polymerization of TP-4C-Azo with PMDA, incorporating 100% photosensitive diamine monomer (as illustrated in **Figure S10a**). GPC analysis revealed that the resulting polymer exhibited a number-average molecular weight (Mn) of 40,860, weight-average molecular weight (Mw) of 45,653,

and a narrow polydispersity index (PDI) of 1.12. Thin films were prepared by spin-coating the polymer solution (initially at 500 rpm for 10 s, followed by 6000 rpm for 60 s) and subsequent thermal treatment in an oven at 80 °C, yielding uniform films with a thickness of 140 nm (**Figure S10b**). The *trans-cis* isomerization kinetics of these Paz films were systematically investigated at five distinct temperatures under constant UV irradiation intensity (3 mW/cm^2).

Preparation of azobenzene polymer films

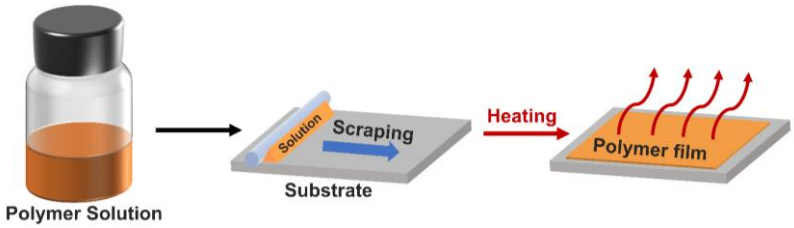

Figure S11. The preparation process of the azobenzene polymer films.

FT-IR, TGA and mechanical properties of azobenzene polymer films with different side-chain structures

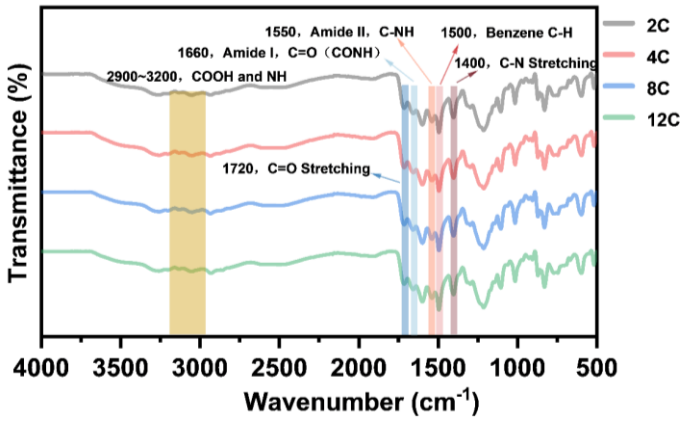

Figure S12. FT-IR spectra of azobenzene-containing polymer films with various side-chain structures.

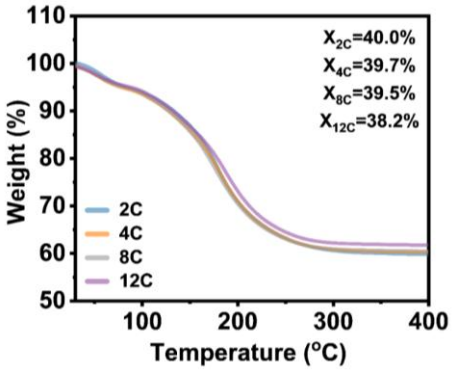

Figure S13. TGA of azobenzene-containing polymer films with various side-chain structures.

Table S5. Young's modulus (GPa) of azobenzene polymer films with different side-chain structures.

Sample ID	2C	4C	8C	12C
1	1.49	1.44	1.39	1.44
2	1.44	1.42	1.42	1.40
3	1.42	1.41	1.49	1.47
4	1.47	1.38	1.43	1.44
5	1.41	1.41	1.46	1.57
Average	1.446±0.034	1.412±0.022	1.438±0.038	1.464±0.064

Photomask specifications

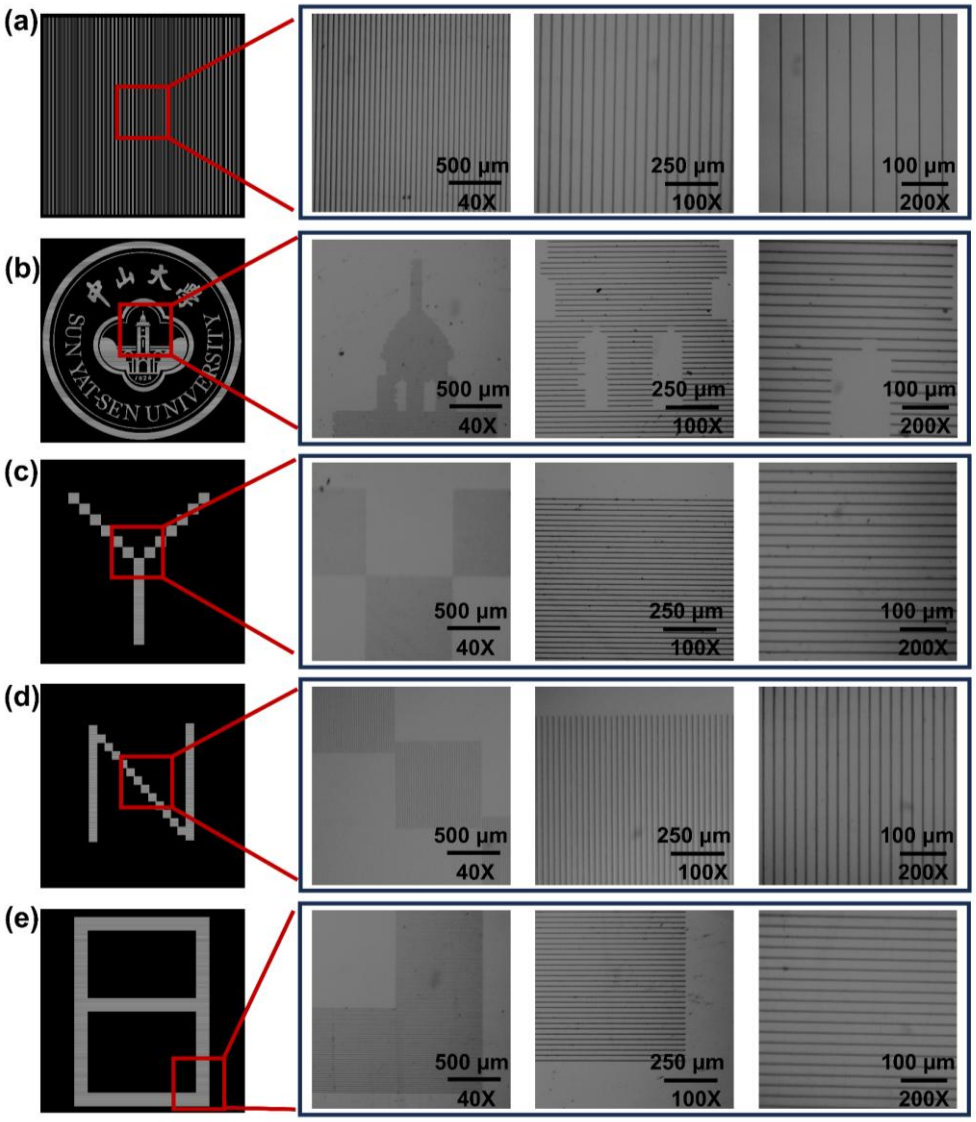

Figure S14. Optical Microscope Images: Pure grating mask template (2-50) (a), the letter 'N' (b), 'Y' (c) and '8' (d), respectively.

Effect of UV exposure time on surface grating morphology

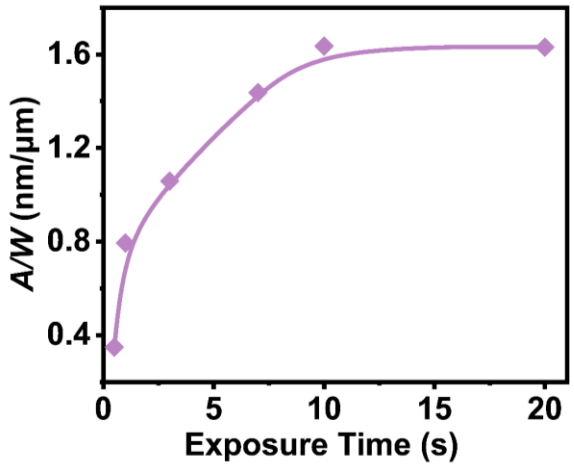

Figure S15. The aspect ratio of the surface gratings on azo polymers varies in accordance with the duration of UV exposure.

Light-induced mass migration in azobenzene polymers

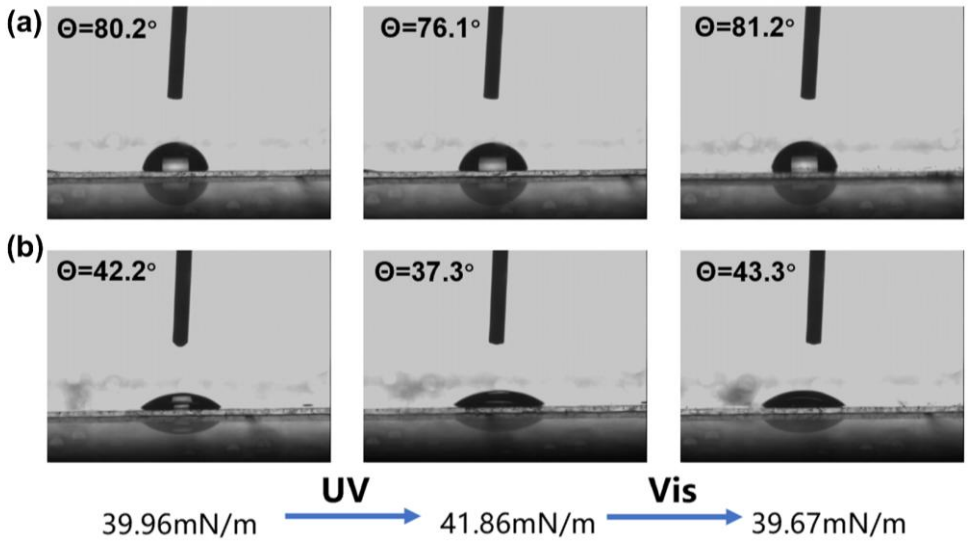

Figure S16. Variations in the contact angles of water (a) and diiodomethane (b), along with the surface energy alterations of the Paz film, without ultraviolet irradiation (A), with ultraviolet irradiation (B), and with visible light irradiation (C).

The surface energy of azobenzene-containing polymeric systems can be modulated under UV irradiation, establishing surface energy gradients (∇_γ) that induce photo-controlled Marangoni flows. These light-induced flows drive the material's inherent molecular motion and deformation. Upon UV exposure through a photomask, the differential surface energy between irradiated and non-irradiated regions generates Marangoni flows, facilitating directional mass migration within the azobenzene-based system. Consequently, this phenomenon results in the spontaneous formation of surface relief gratings on the polymer film surface. To quantitatively evaluate the photo-induced surface energy modifications, we tested the changes in surface energy of the Paz film without ultraviolet irradiation (A), after ultraviolet irradiation (B), and after visible light irradiation (C), as shown in the **Figure S16**. Ultraviolet irradiation reduces the contact angles of water (b) and diiodomethane (c) on the film, leading to an increase in surface energy.

FT-IR, TGA, AFM surface grating morphology, Young's modulus, and the relationship between grating aspect ratio and Young's modulus of azobenzene polymer films with different main-chain structures

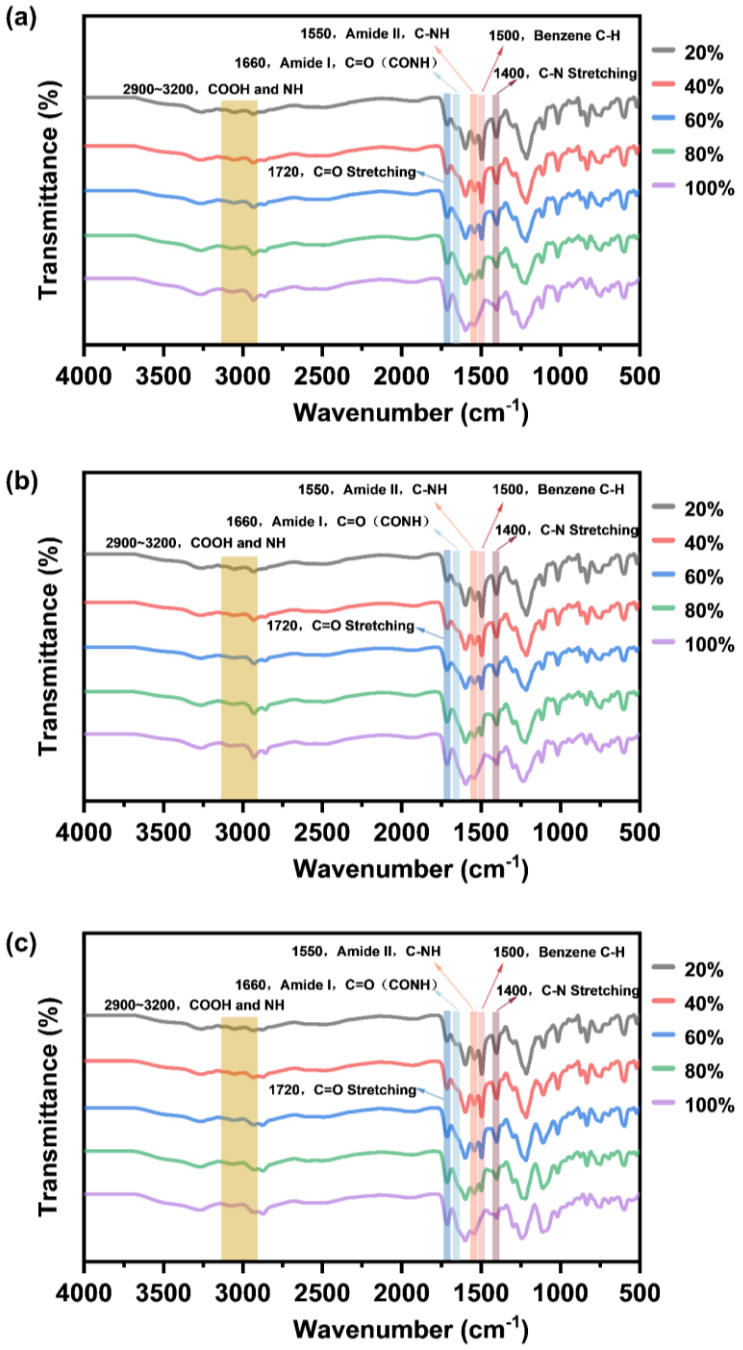

Figure S17. FT-IR spectra of azobenzene polymer films with different contents of HMDA (a), OADA (b), and ZF-NH_2 (c).

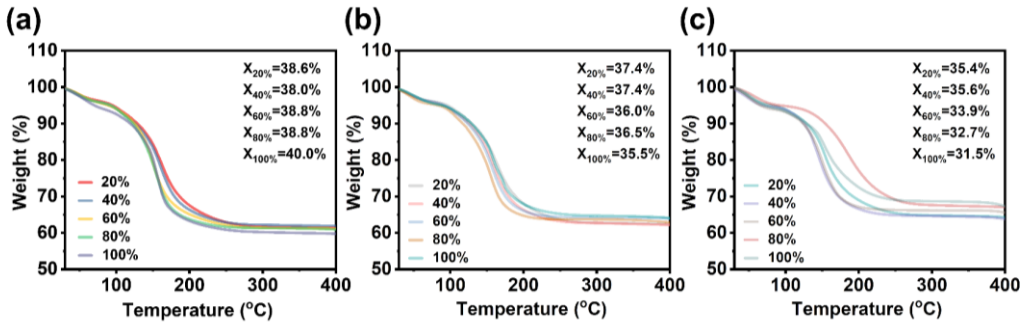

Figure S18. TGA of azobenzene polymer films with different contents of HMDA (a), OADA (b), and ZF-NH_2 (c).

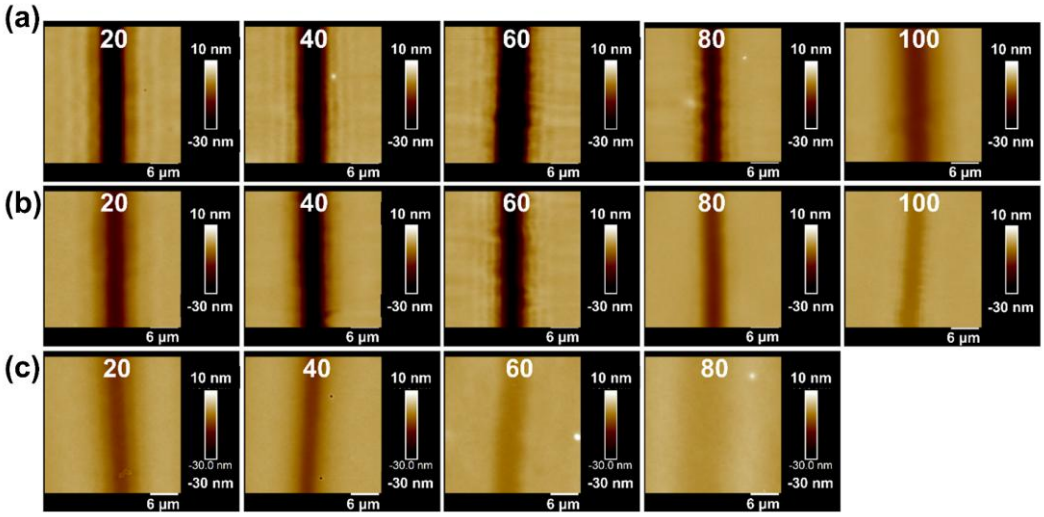

Figure S19. AFM images of surface gratings generated on azobenzene polymer films with different contents of HMDA (a), OADA (b), and ZF-NH2 (c) after identical photomask exposure.

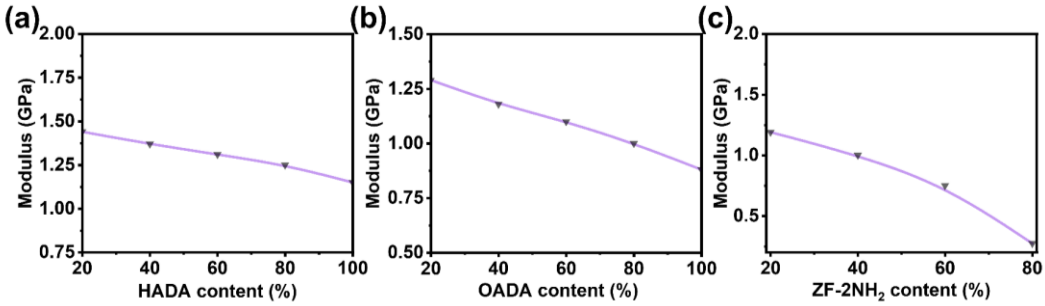

Figure S20. Dependence of Young's modulus on the content of HMDA (a), OADA (b), and ZF-NH_2 (c) in azobenzene-containing polymer films.

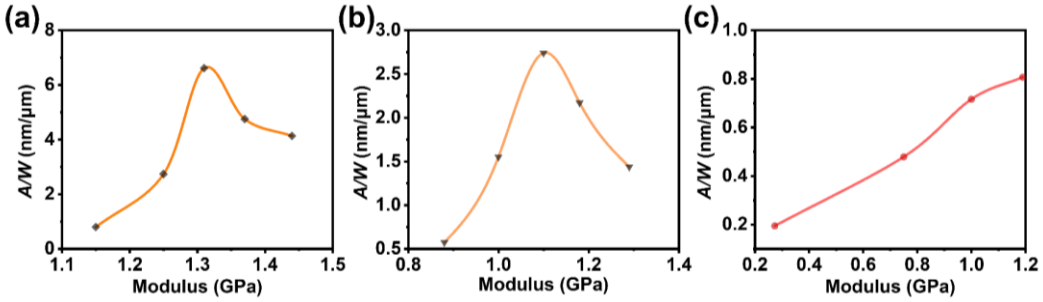

Figure S21. Relationship between surface grating aspect ratio (*A/W*) and Young's modulus for polymer systems with different main-chain flexibility: systems with different contents of (a) HMDA, (b) OADA, and (c) ZF-NH_2.

Photoresponse of spiropyran

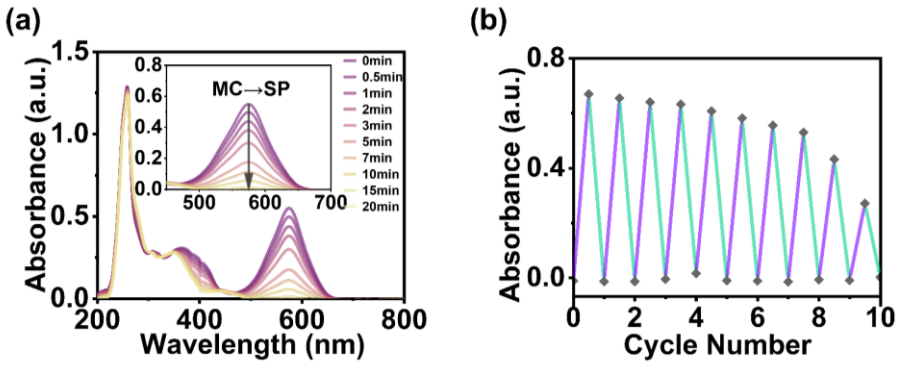

Figure S22. (a) The UV-Vis absorption spectra of purple merocyanine as a function of visible light exposure time. (b) Cycling performance of spiropyran.